International Journal of Mass Spectrometry 478 (2022) 116873

Contents lists available at ScienceDirect

International Journal of Mass Spectrometry

journal homepage: www.elsevier.com/locate/ijms

A unified method for measuring noble gas isotope ratios in air, water, and volcanic gases via dynamic mass spectrometry

Alan M. Seltzer*, David V. Bekaert

Department of Marine Chemistry and Geochemistry, Woods Hole Oceanographic Institution, Woods Hole, MA, USA

ARTICLE INFO

Article history:
Received 18 February 2022
Received in revised form
3 May 2022
Accepted 6 May 2022
Available online 11 May 2022

Keywords:
Isotope ratio mass spectrometry
Noble gas
Isotope geochemistry
Dissolved ga
Atmospheric gases
Mantle volatiles

ABSTRACT

We describe a new method for the purification, transfer, and analysis of heavy noble gas isotope ratios in water, air, or volcanic gas samples using a dynamic dual-inlet isotope-ratio mass spectrometer (IRMS). IRMS noble gas analysis offers the potential for orders-of-magnitude higher precision than traditional (static) noble gas mass spectrometry. However, due to both inherent IRMS requirements and challenges associated with sample collection and purification, measuring noble gases via IRMS has typically been limited to samples with an air-like elemental composition. Our new method allows for highly accurate and precise measurements of Ar, Kr, and Xe isotope ratios via IRMS, independent of sample composition, thereby opening the door to air, water, or volcanic gas analyses all made with the same technique. This approach exploits the fact that purified heavy noble gas samples are dominated by ^{40}Ar, such that matching ^{40}Ar ion beams between sample and reference gas streams results in pressure balancing. We further introduce new techniques for precisely quantifying and correcting for (i) Kr and Xe isotope non-linearity and matrix effects, (ii) interference of the low energy ^{40}Ar tail on ^{36}Ar and ^{38}Ar ion beams, and (iii) the impact of short-term background fluctuations on trace Xe isotope measurements. We also present results from adsorption-desorption experiments with multiple adsorbent materials across a range of temperatures. For adsorption on silica gel, we find small equilibrium isotopic fractionation of Kr ($\varepsilon_{eq} = -0.37 \pm 0.04$‰ amu^{-1}, ±2 SE) and Xe ($\varepsilon_{eq} = -0.06 \pm 0.02$‰ amu^{-1}, ±2 SE) that may be relevant to studies of terrestrial Xe isotope signatures. We demonstrate that adsorption and desorption of heavy noble gases on silica gel at 77 K and 303 K, respectively, is highly reproducible and thus constitutes a viable and efficient method for transferring gases without reliance on cryostats or liquid helium.

1. Introduction

Noble gases are versatile tracers of physical processes in nature due to their chemical and biological inertness. Applications of noble gases in the geosciences are far ranging, from constraining planetary volatile origins and geochronology with noble gases trapped in rocks to quantifying past climate conditions based on noble gases in occluded ice core air bubbles or dissolved in ancient groundwater. Since the early 20th century, analytical techniques for measuring noble gases have grown hand-in-hand with mass spectrometry. In fact, the discovery of neon isotopes (^{22}Ne and ^{20}Ne) is associated with the advent of mass spectroscopy itself [1].

Today, there are two primary techniques for noble gas analysis: static and dynamic mass spectrometry. Both techniques involve sector-field, gas-phase mass spectrometers with Nier-type sources [2]. With a static mass spectrometer [3–5], commonly referred to as a "noble gas mass spectrometer," a purified gas sample is first introduced a single time and then consumed over time as it is ionized. This technique is suitable for extremely small samples, such as noble gases trapped in rocks, and it has been widely used for geological applications including K–Ar and Ar–Ar dating [6] and studies of the sources of crustal and mantle volatiles [7]. Conversely, with a dynamic mass spectrometer, often called an "isotope ratio mass spectrometer" (IRMS), purified noble gases continuously flow from a dual inlet, which consists of two variable volumes containing sample and reference gases, into either an ion source that is dynamically pumped or to a waste line. Rapid switching between analysis of sample and reference gas streams reduces the effect of instrumental drift [8] and thereby greatly enhances analytical precision. Dynamic mass spectrometry requires orders-of-magnitude more gas than static mass spectrometry to ensure sufficiently high pressure and thus viscous flow from

* Corresponding author.
E-mail address: aseltzer@whoi.edu (A.M. Seltzer).

https://doi.org/10.1016/j.ijms.2022.116873
1387-3806/

the inlet bellows. For this reason, application of dynamic mass spectrometry for noble gas analysis has largely been limited to gas-rich samples like ice core air bubbles [9].

In addition to needing large volumes of gas, dynamic measurements require that the total gas pressure is balanced between sample and reference bellows to ensure similar flow dynamics and ion beam intensities. Thus, any physical fractionation or non-linearity in ion beams is largely canceled out since it affects sample and reference gases equally. Existing techniques for high-precision dynamic noble gas isotope measurements and corrections for non-linearity and matrix effects [9,10] have grown out of techniques for measurement of O_2 and N_2 elemental and isotopic ratios in air [11,12]. Because the elemental ratios of sample and reference gases are air-like in each of these techniques, measurement of trace gases is straightforward without violating the requirement for balanced sample and reference gas pressures. For example, if one were to measure Xe isotopes in an air-like purified noble gas sample, with an air-like reference gas, ion beam intensities and total gas pressure would be similar in both sample and reference bellows because they have similar Xe/Ar ratios. However, if one were to measure Xe isotopes in purified dissolved gases from a water sample (Xe/Ar ratio roughly three times higher than air) using an air-like reference gas and balancing ^{132}Xe beam intensities before analysis, the total gas pressure would be roughly three times lower in the sample bellows than in the reference bellows. With unbalanced flows, differences in physical fractionation between the bellows, and space charge and ion-molecule interactions in the ion source, can lead to large biases. To circumvent this issue, a recent study analyzed dissolved noble gases using a reference gas with air-equilibrated water (AEW)-like elemental noble gas ratios [13]. However, regularly switching between water-like and air-like reference gas cans is impractical for routine analysis of both air and water samples, and for samples in which noble gas elemental ratios are unknown *a priori* (e.g., volcanic gases) there presently exists no method for dynamic measurement of noble gas isotopes while assuring balanced flow.

Here we introduce a new unified technique that permits analysis of heavy noble gas isotopes (Ar, Kr, and Xe) in air, water, and volcanic gases via dynamic mass spectrometry without prior knowledge of elemental ratios. Our approach makes use of the fact that ^{40}Ar comprises over 99.5% of the total gas content of any air, water, or volcanic gas sample that has undergone quantitative purification, such that all reactive gases and helium are removed. Thus, by balancing sample and reference ^{40}Ar beams, total gas pressures are similarly balanced. This technique allows for highly accurate and precise isotope ratio measurements of Ar (^{40}Ar, ^{38}Ar, ^{36}Ar), Kr (^{86}Kr, ^{84}Kr, ^{82}Kr), and Xe (^{136}Xe, ^{134}Xe, ^{132}Xe, ^{131}Xe, ^{130}Xe, ^{129}Xe, ^{128}Xe) via dynamic mass spectrometry, independent of Ar/Kr and Ar/Xe ratios. However, it requires robust corrections for matrix effects, fluctuations in Faraday cup background voltages that impact the rarest isotopes, and isobaric interference of ^{38}Ar and ^{36}Ar by the low energy ^{40}Ar tail. In thus study, we describe each of these important corrections and introduce a new gas purification system that accommodates air, water, and volcanic gases while using Si gel cooled by liquid nitrogen (77 K) for gas transfer, thereby eliminating the need for a cryostat or liquid helium. Finally, we present the results of experiments testing the elemental and isotopic effects of using different adsorbent materials at different temperatures to transfer noble gases from the purification system to an IRMS.

2. Materials and methods

Here we describe the full sequence of steps involved in heavy noble gas measurements via IRMS, including purification of gas samples, transfer from the purification system to the IRMS in silica gel-containing dual-valve dip tubes, IRMS analysis, and the application of a series of analytical corrections. All sample processing and analysis was performed in the Seltzer Lab in the Department of Marine Chemistry and Geochemistry at Woods Hole Oceanographic Institution (Woods Hole, MA, USA).

2.1. Sample purification and transfer

Before analysis via dynamic mass spectrometry (described in Section 2.2), all samples and standards are purified and transferred to the IRMS following an identical protocol. As shown in Fig. 1, the extraction line consists of a series of valves, dilution volumes, as well as gauges, a water trap, a silica gel trap, a getter furnace, and a dual-valve dip tube (far right). High vacuum ($<10^{-4}$ Torr) is maintained by an Edwards 75DX turbomolecular pump backed by an Edwards nXDS 6i scroll pump, with a bypass valve such that the scroll pump can also be used to rough pump the extraction line. The dilution volumes are interchangeable, but a 100 mL glass bulb is always used for air standards. The silica gel trap is a 3/4" diameter stainless steel tube filled with 50 silica gel granules (Thermo Scientific, −3+8 mesh) and has a heating coil on the outside, which is connected to a variable transformer. The water trap (Ace Glass 8670) is immersed in an ethanol/liquid N_2 slurry and monitored to maintain a temperature between −80 and −100 °C. The getter furnace consists of a 1/2″ diameter quartz tube (Ace Glass 8683) containing ~4 g of Ti sponge (Alfa Aesar 3 mm) that is positioned inside a ceramic cylinder heater (Watlow VC400N06A) that is connected to a separate variable transformer and mounted to a movable rack so that the tube can be removed, and the getter material replaced, between samples. There are three pressure gauges on the line: two Granville-Phillips 275 Convectron gauges to either monitor backing pressure behind the turbomolecular pump (convectron 1) or leak check the main line (convectron 2), and one 1000 Torr MKS Baratron capacitance manometer used to roughly estimate sample size and monitor gettering progress. Finally, detachable dip tubes are connected to the line (far right in Fig. 1) and used to transfer Ar, Kr, and Xe from the purification line to the IRMS. The dip tubes each consist of two Swagelok 4BG bellow sealed valves that isolate a main stainless-steel chamber (~10 mL) from a smaller volume (~1 mL) filled with ten silica gel granules.

The overall goal of sample processing is to isolate the heavy noble gases in a gas sample (e.g., air, extracted dissolved gases from water, or volcanic gas) connected to the left side of the extraction line in Fig. 1, remove all reactive gases (e.g., N_2, O_2, CO_2, hydrocarbons), and transfer the Ar, Kr, and Xe quantitatively into the detachable dip tube on the right side of the line. The dip tube is initially evacuated, with valve VT2 open. After the sample and dip tube are connected, the line is pumped to high vacuum and leak checked by closing valve TP, which isolates the line from the turbomolecular pump. To proceed, the apparent leak rate must be below 10^{-4} Torr min^{-1} measured on convectron 2 in Fig. 1 (a Granville-Phillips 275 Convectron gauge). After passing a leak check, the getter oven is heated to 900 °C while being pumped to precondition the Ti sponge. Next, valve 5 is closed, forcing the sample to pass through the water trap, and valves TP, FV, ST, GO, DT, and CV are also closed to isolate the interior of the vacuum line. Valves 2 and 3 may be opened or closed, depending on the desired dilution and whether the sample contains multiple replicate aliquots of gas that will each be processed separately. (Note: valve 1 is open by default after the sample is connected, it is assumed that sample flasks have their own valves.) The sample is introduced by opening the valve on the sample flask and the Baratron pressure is noted. Gettering proceeds in two stages: a first stage in which gas is quickly drawn into a smaller volume, expanded, and gettered to

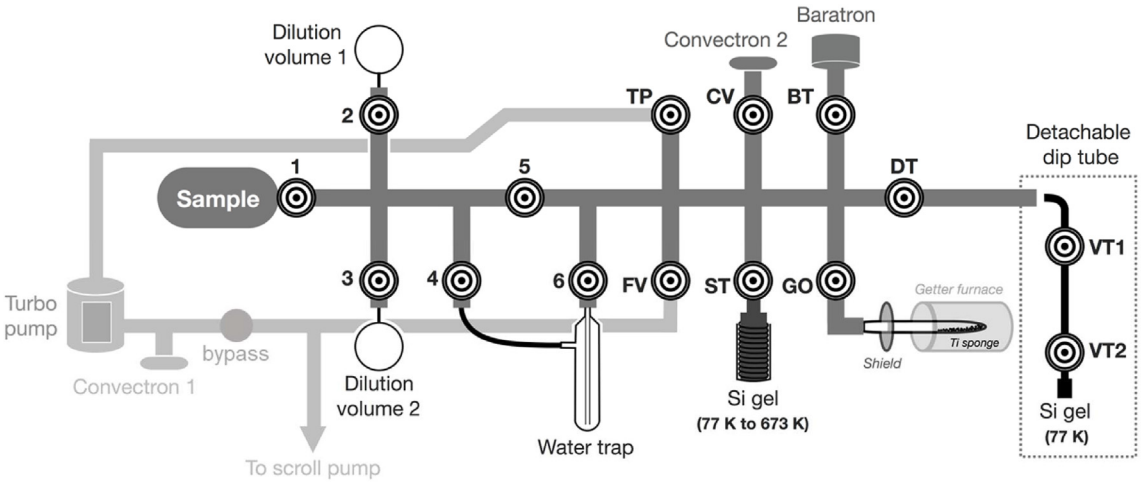

Fig. 1. Overview of gas extraction, purification, and transfer system. Numbered concentric circles indicate valves (Swagelok 4BG), while all other labeled components are pumps, gauges, traps, a getter furnace, glass volumes for dilution, a bypass valve between the scroll and turbomolecular pumps, a sample flask, or the detachable dip tube. The abbreviations TP, FV, ST, CV, BT, GO, and DT refer to valves that isolate the turbo molecular pump, fore pump, in-line silica gel trap, Convectron gauge, Baratron manometer, getter oven, and dip tube, respectively. The labels VT1 and VT2 refer the outer and inner valve on the detachable dip tube, respectively.

~80% completion, and a second stage in which the gas is quantitatively transferred onto the silica gel trap, released into a small volume, and getter for 2.5 h. At the beginning of the first stage, the sample is partially gettered for 5 min by opening GO and the Si gel trap is immersed in liquid N_2 (77 K), with valve ST remaining closed. After 5 min, the pressure is noted, valve ST is opened, and 5 min are given for initial sample trapping on the Si gel. The pressure is then noted, valve 6 is closed, the N_2 dewar is removed and the Si gel trap is heated to 400 °C. At this point, typically over 95% of the total gas has either been gettered or trapped on the Si gel, such that when it is released into the smaller volume (~50 mL) of the line with valve 6 closed, the pressure is high and gettering is most efficient. Gettering proceeds for 10 min, after which the Si gel heating coil is switched off and re-immersed in liquid N_2. The second stage then begins with 5 min of re-trapping on the Si gel, after which the pressure is noted (usually close to the baseline), valve 6 is re-opened, and 15 min are given to trap any residual gas that was not initially trapped or gettered. After 15 min, valves 6 and ST are closed, the pressure is noted, and valve TP is opened to remove incondensable gases (e.g., He in the case of volcanic gas samples). In a sample that is not expected to have appreciable He or H_2 content (e.g., air), the pressure should not change when valve TP is opened, and this step thus serves as a useful internal check for air standards. Valve TP is then closed again, valve ST is opened, the liquid N_2 dewar is removed, and the Si gel trap is heated to 400 °C once again to getter the remaining reactive gases thoroughly. After 2.5 h, the pressure is noted and the getter oven is switched off and moved to the back of the quartz tube, allowing 10 min for removal of any H_2 that has been produced by gettering. During this period, the bottom Si gel chamber of the dip tube is immersed in liquid N_2. Next, the pressure is noted, and valves DT and VT1 are opened, beginning the transfer of heavy noble gases into the dip tube. After 15 min, valve VT1 is closed, the pressure is noted (it should be at the baseline) and valve TP is opened as a check that no gases remain in the line. Finally, valve DT is closed, and the line is prepared for the next sample (e.g., Ti sponge replaced, Si gel trap cooled to room temperature, line pumped back to high vacuum). The dip tube is then placed in a 30 °C water bath, where noble gases desorb from the Si gel and reach equilibrium over a period of at least 3 h. After this period, valve VT2 is closed, the dip tube is removed from the water bath, dried, and connected to the dual-inlet system of the IRMS.

In this study, we distinguish between samples, standards (air or AEW), and reference gases in the following manner: samples and standards are initially unpurified gases that undergo gettering to remove all reactive gases before being transferred to the IRMS in a dip tube, while reference gases are pure noble gases in stainless steel cans with aliquoting chambers that can be directly connected to the IRMS dual-inlet system. All samples, standards, and reference gases yield ~1 mL_{STP} of pure noble gases (of which >99.5% is ^{40}Ar) with variable Ar/Kr and Ar/Xe ratios. We use two reference cans, called RC0 and RC25, each of which consists of 2 L stainless steel cylinder connected to a 2.5 mL aliquoting chambers isolated on both sides by Swagelok 4BG bellows-sealed valves. Reference can RC25 is always connected to the dual-inlet system, thus serving as the permanent reference for IRMS analysis. Both cans contain mixtures of pure Ar, Kr, and Xe at ~300 Torr total pressure, and both cans have a ~800:1 reservoir-to-aliquot volume ratio. The Ar/Kr and Ar/Xe ratios of RC25 and RC0 approximately resemble 25 °C and 0 °C AEW, respectively. Air standards consist of ~100 mL_{STP} of laboratory air that is introduced to the extraction system and processed identically to any sample. AEW standards are collected by equilibrating a 9 L reservoir of deionized water with continuously flowing, humidified laboratory air following the method of Jenkins et al. [14]. For each AEW sample, approximately 2.5 L of water is collected into a 6 L flask (Restek TO-Can with a Swagelok 4H bellows valve) that is subsequently equilibrated in an isothermal chamber on an orbital shaker at 50 rpm for a minimum of three days before the water is drained, leaving only the headspace and ~30 mL of residual water following the method of Emerson et al. [15]. As in Emerson (1999), solubility equilibrium corrections are made for the fraction of Ar, Kr, and Xe dissolved in the flasks, as well as the small residual water after draining, using most current elemental and isotopic solubility values [13,14]. Close agreement between measured $^{40}Ar/^{36}Ar$ ratios in AEW standards and published equilibrium values (root-mean-square deviation = 0.012‰; $n = 16$) indicates that AEW standards achieve full solubility equilibrium with negligible isotopic fractionation. Although all samples and standards are analyzed against a common reference gas (R25), final isotope ratios are ultimately reported with respect to the mean values of air standards because any potential biases during purification, transfer, and analysis should affect samples and standards equally.

2.2. IRMS analysis

Purified samples and standards were measured using a Thermo MAT 253 plus equipped with 10 Faraday cups that allow for simultaneous detection of either Ar, Kr, or Xe isotopes depending on the magnetic and electrical field strengths. An overview of the amplification, typical beam intensities, and elemental and isotopic abundances of the 13 noble gas isotopes analyzed with this technique is provided in Table 1. The analytical techniques and corrections used in this study generally follow existing IRMS techniques for inert gas isotopes [9,10,13], with several important modifications.

First, as described previously, balancing of pressure between sample and reference bellows is achieved by compressing the bellows such that the ^{40}Ar ion beam intensity reaches a target value of 6650 mV (3×10^8 Ω resistor). To measure Ar isotopes, analysis begins immediately after pressure balancing, whereas to measure Kr or Xe isotopes, magnetic peak jumping is employed after pressure balancing, and electric peak centering is then performed using either the ^{84}Kr or ^{132}Xe peaks for alignment.

Second, to accommodate a wide range of sample sizes and minimize the overall impact of small pressure imbalances between the bellows, pressure readjustment takes place after eight integration cycles. We define a set of contiguous integration cycles, separated by pressure rebalancing, as a "block." An integration "cycle" consists of a sample gas measurement made in between two reference gas measurements. We define integration time (T_{int}) as the duration of time when ion beams are measured (for either sample or reference gas) and idle time (T_{idle}) as the duration of time after switching between gas streams before integration begins. A summary of measured isotope ratios and their associated bellows run pressure, integration times, idle times, number of total integration cycles per typical analysis, measurement uncertainties in air and water, and correction factors for pressure imbalance and matrix effects (describe in Section 2.3) is provided in Table 2. A typical analysis consists of six Ar blocks (48 cycles), eight Kr blocks (64 cycles), and twelve Xe blocks (96 cycles). Importantly, this method allows for measurement of smaller samples, for which fewer blocks can be measured.

Third, intermediate masses are measured on unused Faraday cups situated in between the ^{36}Ar, ^{38}Ar, and ^{40}Ar to record and ultimately correct for interference by the low energy tail of ^{40}Ar. This tail correction is described and demonstrated in Section 2.3.4. A final key modification to prior techniques is the processing of sample data. A MATLAB subroutine was developed to process raw output from Thermo's ISODAT software, enabling (i) automated determination of Kr/Ar and Xe/Ar ratios by back-projecting ^{84}Kr and ^{132}Xe beam intensities recorded throughout a measurement block to the time of ^{40}Ar pressure balancing, and (ii) long-term tracking of important parameters including the pressure and ^{40}Ar ion beam intensities of the sample and reference bellows at the time of pressure balancing (which facilitates convenient logging of instrument sensitivity over time) as well as the background Faraday cup voltages recorded before and after each analysis.

To analyze a sample, a dip tube or reference gas can is first connected to the sample side of the dual-inlet system and the inlet is pumped to high vacuum and leak checked. Next, an aliquot of reference gas is equilibrated within the reference gas can for 10 min. The reference gas aliquot and sample aliquot are then introduced to their respective bellows, allowing for 10 min of equilibration. Finally, the bellows are isolated and analysis begins. Before the first block of analysis of each element (Ar, Kr, or Xe), the ion source is completely isolated from the inlet and, after 60 s, background voltages are recorded on all Faraday cups by integrating for the duration of one integration cycle. These background voltages are then subtracted automatically from all measurements by Thermo's ISODAT software in reporting ion beam intensities. Ar isotope blocks are measured first, followed by Kr isotope blocks and then Xe isotope blocks. Finally, at the end of the measurement, $^{28}N_2$ is measured by peak jumping as a first-order check on sample purity. Typical $^{28}N_2$ beam intensities in air standards are <1000 mV, measured on a $1 \times 10^{11}\Omega$ resistor at 30 mbar pressure. At 30 mbar, ^{40}Ar beam intensity is 6650 mV as measured on a 3×10^8 Ω resistor, indicating that typical gettered air standards have N_2/Ar ratios on the order of 10^{-4} (assuming Ar and N_2 have ionization efficiencies on the same order of magnitude), implying that gettering results in the successful removal of ~99.999% of N_2 (the N_2/Ar ratio of air is ~83.6). A typical measurement (i.e., with the number of integration cycles of Ar, Kr, and Xe listed in Table 2) takes roughly 7 h to complete.

In this study we present IRMS data using δ notation,

$$\delta = \frac{R_{sample}}{R_{standard}} - 1 \quad (1)$$

where R_{sample} is an isotopic or elemental ratio measured in a sample and $R_{standard}$ is the same ratio measured in either (i) air or (ii) the working reference gas R25. We conventionally report δ values as ‰ deviations from air or R25 in this study. We report the reproducibility (±1σ) of isotope ratio measurements in air standards (n = 26) and AEW standards (n = 16) in Table 2. For any single analysis, the reported δ value for each isotopic or elemental ratio of interest represents the mean of all integration-cycle δ values, corrected for four sources of random or systematic error: (i) fluctuations in the background voltages of Faraday cups that introduce small random errors that become appreciable for ratios involving trace Xe isotopes; (ii) matrix effects, wherein the combination of multiple processes leads to a systematic bias in Kr or Xe isotope ratios as a function of the Ar/Kr or Ar/Xe ratio of the sample; (iii) pressure imbalances between the sample and reference bellows, which induce small systematic biases associated with instrumental nonlinearity; and (iv) isobaric interference of the ^{36}Ar and ^{38}Ar ion beams with the low-mass tail of the ^{40}Ar ion beam. We describe each of these corrections in detail in the following section.

Table 1
Overview of 13 heavy noble gas isotopes measured in this study, including the magnitude of ion beam amplification and beam intensities in air and water, and elemental and isotopic abundances.

	^{40}Ar	^{38}Ar	^{36}Ar	^{86}Kr	^{84}Kr	^{82}Kr	^{136}Xe	^{134}Xe	^{132}Xe	^{131}Xe	^{130}Xe	^{129}Xe	^{128}Xe
Amplification (Ω)	3×10^8	10^{12}	10^{11}	10^{13}	10^{13}	10^{13}	10^{13}	10^{13}	10^{13}	10^{13}	10^{13}	10^{13}	10^{13}
Beam intensity, air (V)	6.6	13.7	7.0	6.1	20.6	3.9	0.7	0.8	2.2	1.8	0.3	2.1	0.2
Beam intensity, 22ºC water (V)	6.6	13.7	7.0	10.8	36.4	7.0	2.2	2.6	6.6	5.5	1.0	6.4	0.5
Bulk elemental mixing ratio, dry air	9.34×10^{-3}			1.14×10^{-6}			8.7×10^{-8}						
Isotope abundance, air (%)	99.6	0.06	0.33	17.3	57.0	11.6	8.9	10.4	26.9	21.2	4.1	26.4	1.9

Table 2
Summary of IRMS analysis parameters, sample precision, and correction factors for isotopic ratios of interest. P_{run} refers to the bellows pressure during IRMS analysis; n_{cycles} refers to the total number of integration cycles for a given isotope ratio during a typical sample measurement; T_{idle} and T_{int} are idle and integration times, respectively; σ_{air} and σ_{h2o} are air and AEW standard 1-σ reproducibilities, respectively; PIS refers to pressure imbalance sensitivity; and ME refers to matrix effect correction factor.

	$^{40}Ar/^{36}Ar$	$^{38}Ar/^{36}Ar$	$^{86}Kr/^{82}Kr$	$^{86}Kr/^{84}Kr$	$^{136}Xe/^{129}Xe$	$^{134}Xe/^{129}Xe$	$^{132}Xe/^{129}Xe$	$^{131}Xe/^{129}Xe$	$^{130}Xe/^{129}Xe$	$^{128}Xe/^{129}Xe$
Δm (amu)	4	2	4	2	7	5	3	2	1	−1
P_{run} (mbar)	30	30	22	22	30	30	30	30	30	30
n_{cycles}	48	48	64	64	96	96	96	96	96	96
T_{idle} (s)	8	8	15	15	18	18	18	18	18	18
T_{int} (s)	10	10	20	20	22	22	22	22	22	22
σ_{air} (‰)	0.007	0.009	0.030	0.017	0.079	0.059	0.061	0.076	0.076	0.136
σ_{h2o} (‰)	0.012	0.017	0.023	0.018	0.029	0.027	0.017	0.032	0.044	0.071
PIS (10^{-4})	2.9 (±0.5)	1.3 (±1.3)	3.0 (±3.0)	0.8 (±2.5)	10.1 (±4.7)	5.6 (±4.4)	0.8 (±3.4)	0.5 (±3.4)	19.0 (±6.5)	−8.5 (±10.3)
ME (10^{-5})	–	–	2.5 (±1.6)	9.1 (±1.1)	14.9 (±0.9)	12.3 (±1.0)	8.5 (±0.6)	16.1 (±1.1)	1.3 (±1.1)	24.8 (±1.6)

2.3. Analytical corrections

2.3.1. Background fluctuations

A novel aspect of this new technique is the inclusion of three more Xe isotopes (^{131}Xe, ^{130}Xe, ^{128}Xe) than prior Xe IRMS studies [13,16–19]. The inclusion of the trace isotopes ^{128}Xe and ^{130}Xe, which are respectively ~4 and ~2 times less abundant than ^{136}Xe (the least abundant Xe isotope measured in prior studies), raises important concerns about the high sensitivity of trace Xe isotopes to small variations in measured ion beam intensities (e.g., due to Johnson noise in Faraday cup amplifiers). That is, a given error in a measured background intensity (which is subtracted from a measured ion beam intensity) will lead to a correspondingly larger fractional error for less abundant isotopes with smaller ion beams.

To investigate the impact of background fluctuations on trace Xe isotope measurements, we explored variability in background intensities measured on the Faraday cups that detect ^{128}Xe, ^{130}Xe, ^{134}Xe, and ^{136}Xe ion beams (the four least abundant Xe isotopes that we measure) throughout 195 total measurements from May through December 2021. Note that all four of these isotopes are measured with the same magnitude of amplification (10^{13} Ω). Fig. 2 shows background beam intensities (BG) and anomalies (BG′) of measured BG intensities from a spline fit of each isotope's background time series (smoothing parameter = 0.0005). We find no temporal trend in BG′ for any isotope, and we observe that the sample-to-sample deviation in background intensities is quite consistent among all four isotopes, with standard deviations of BG′ equal to 0.10, 0.11, 0.15, and 0.14 mV for ^{128}Xe, ^{130}Xe, ^{134}Xe, and ^{136}Xe, respectively. Given that BG′ data for different isotopes are uncorrelated with similar standard deviations despite considerable variation among these four isotopes in isotopic abundance (Table 1), we suggest that sample-to-sample differences in background intensities reflect uncorrelated electronic noise on each detector cup, rather than differences in detection of actual background Xe or other isobaric contaminants in the instrument.

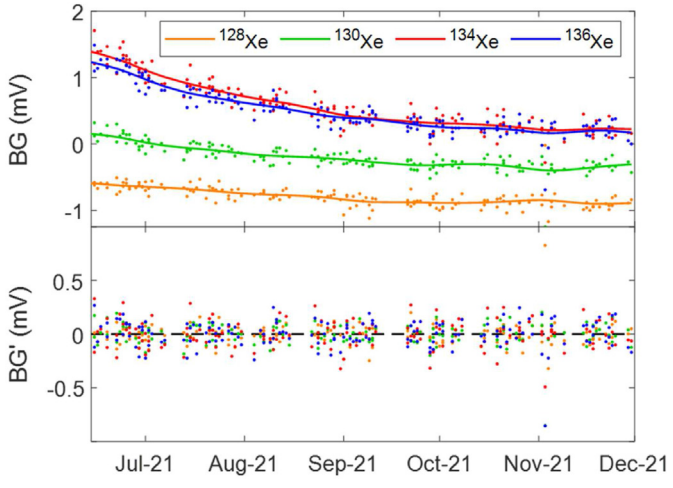

Fig. 2. Time series of background intensities (BG, top panel) and anomalies (BG′, bottom panel) from a spline fit to background data recorded at the beginning of Xe analysis for 195 sample measurements from May through December 2021. (Note that the sign and absolute magnitude of BG values are not meaningful, as they include arbitrary offsets from zero and thus result in some negative values.)

In Fig. 3, we compare anomalies of measured Xe isotope ratios in air (Xe/Ar ratio ~10^{-6}) to background anomalies associated with each air standard measurement. In Fig. 3, each data point represents an individual air standard BG' value and δ anomaly (from the mean of 26 air standards), where each trace Xe isotope is normalized to ^{129}Xe. We normalize to ^{129}Xe both because of prior convention (e.g., Ref. [16] and because ^{129}Xe is ~2.5–~14 times more abundant than these four rarer Xe isotopes and thus is less sensitive to background fluctuations. We find significant correlations for all four isotope ratios with regression coefficients (slopes) that scale with the atmospheric abundance of the rarer of the two Xe isotopes in each ratio. Crucially, the slope of each linear regression is negative, such that positive δ anomalies are associated with negative background anomalies. This observation of negative slopes that scale with isotopic abundance in air is consistent with the notion that subtraction of erroneous background intensities from isotope measurements leads to corresponding random errors in δ values. That is, if a background measurement for ^{128}Xe is erroneously high and this value is subtracted from measured ^{128}Xe beam intensities for a given sample, then the $^{128}Xe/^{129}Xe$ ratio for this sample (neglecting any background-related error in ^{129}Xe because of its high abundance) will appear erroneously low. If background errors are similar in magnitude for all detector cups (as appears to be the case; Fig. 2), then the ^{129}Xe-normalized ratios with the least abundant isotopes in the numerator will be the most affected, as we observe.

We introduce a correction, β, for background-induced error in δ values by making use of the fact that these anomalies are small (<1‰) and thus δ values are additive to good approximation:

$$\beta_i = \frac{BG'_i}{V_{R,i}} - \frac{BG'_i}{V_{SA,i}} \quad (2)$$

where i corresponds to a trace Xe isotope (^{128}Xe, ^{130}Xe, ^{134}Xe, or ^{136}Xe), BG' is the background anomaly (mV), V_{SA} is the measured sample gas ion beam intensity (mV) of isotope i, and V_R is the measured reference gas ion beam intensity (mV) of isotope i. The background correction is applied as follows for a measured $^{i}Xe/^{129}Xe$ ratio ($\delta^{i}Xe/^{129}Xe_{meas}$):

$$\delta^{i}Xe/^{129}Xe_{BG-corrected} = \delta^{i}Xe/^{129}Xe_{meas} - \beta_i \quad (3)$$

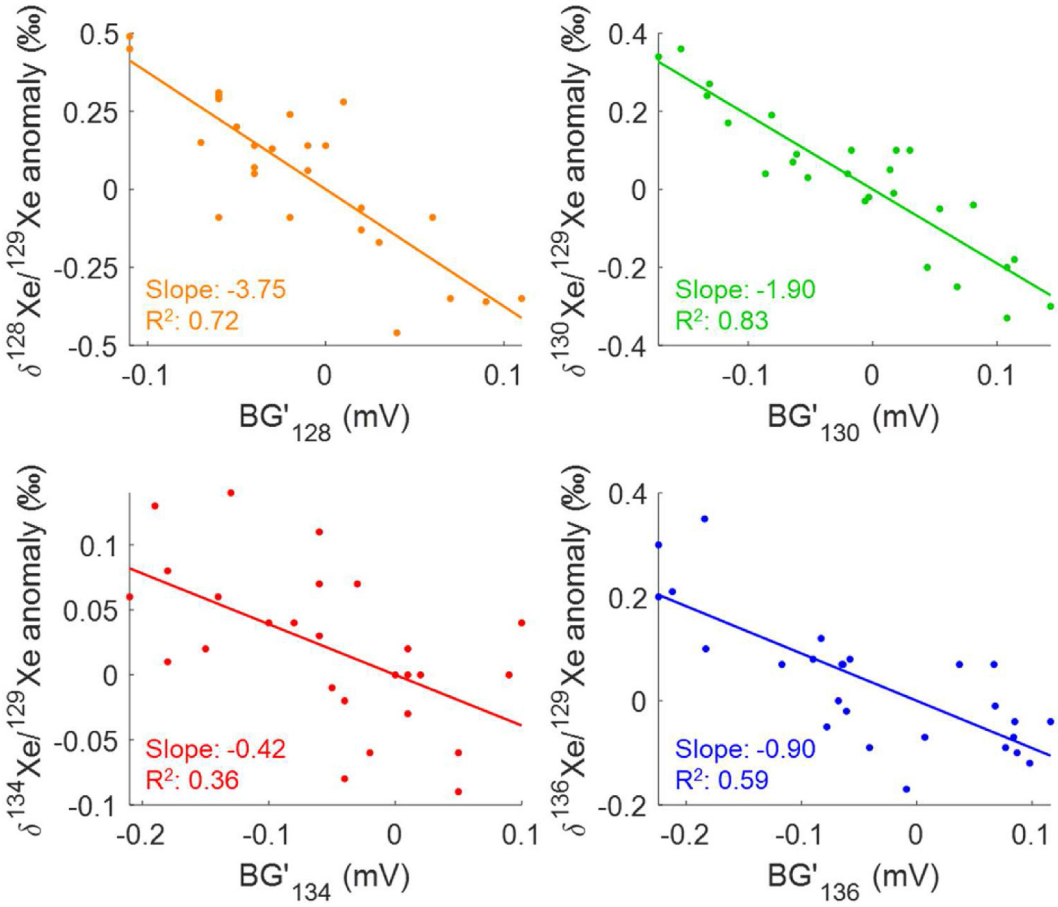

Fig. 3. Comparison of Xe isotope anomalies in air-standard measurements and associated background error for the four rarest Xe isotopes measured (normalized to ^{129}Xe). An isotope ratio anomaly refers to a measured δ value minus the mean of all air-standard measurements (n = 26). A background error (BG'; subscript refers to a rare Xe isotope mass) is the associated anomaly of a background measurement from the long-term trend, as shown in Fig. 2. Slopes and R^2 values for each isotope ratio refer to linear regressions with zero intercept.

By correcting air and AEW samples in this manner, we find that sample reproducibility improves considerably for all isotope ratios except for ^{134}Xe/^{129}Xe, which is essentially unchanged. For air standards (n = 26), corrected (uncorrected) 1-σ reproducibilities are 0.136 (0.252)‰, 0.76 (0.186)‰, 0.59 (0.060)‰, and 0.79 (0.126)‰ for ^{128}Xe/^{129}Xe, ^{130}Xe/^{129}Xe, ^{134}Xe/^{129}Xe, and ^{136}Xe/^{129}Xe, respectively. Because background corrections are negligible for ^{134}Xe/^{129}Xe in air and AEW, we do not attempt to correct ^{131}Xe, ^{132}Xe, or ^{129}Xe for background-related errors, as each of these isotopes is at least twice as abundant as ^{134}Xe and would thus require an even smaller background correction. We discuss the importance of background corrections, the origin of errors in the measured background (Johnson noise) and speculate about strategies for minimizing these corrections in Section 3.2.

2.3.2. Matrix effects

The bulk composition of gas is well known to influence the apparent isotope ratios of individual gases in a mixture. For example, prior studies employing an IRMS to measure inert gas mixtures have empirically determined, and corrected for, changes in isotopic ionization efficiency due to changes in bulk gas ratios between sample and reference gases. For example, Severinghaus et al. [9] determined a "chemical slope" to correct measured δ^{40}Ar/^{36}Ar for sample versus reference gas differences in the N_2/Ar ratio in ice core and air samples. Past studies employing chemical slope corrections have demonstrated the suitability of linear corrections over a wide range of changes in bulk gas composition [9,13]. In this technique, differences in the Ar/Kr and Ar/Xe ratios between sample and reference gases similarly lead to linear biases in measured Kr and Xe isotope ratios that require a chemical-slope correction. Additionally, because we pressure balance sample and reference gases using ^{40}Ar beams, the Ar/Kr and Ar/Xe ratios of a sample also influence the ion beam intensities of Kr and Xe isotopes. That is, Xe isotope beam intensities will be higher in a sample with a lower Ar/Xe ratio when pressure balancing is performed using the ^{40}Ar ion beam. Consequently, measured Kr and Xe isotope ratios can be impacted in two ways due to the Ar/Kr and Ar/Xe ratios of a sample, both by the chemical slope effect and instrumental nonlinearity. In this study, we refer to the combined influence of these effects as matrix effects (ME), and we corrected measured Kr and Xe isotope ratios as follows:

$$\delta^i\mathrm{Kr}/^j\mathrm{Kr}_{\mathrm{ME-corrected}} = \delta^i\mathrm{Kr}/^j\mathrm{Kr}_{\mathrm{meas}} - ME_{ij} \times \delta Ar \Big/ Kr \quad (4)$$

or

$$\delta^i\mathrm{Xe}/^j\mathrm{Xe}_{\mathrm{ME-corrected}} = \delta^i\mathrm{Xe}/^j\mathrm{Xe}_{\mathrm{meas}} - ME_{ij} \times \delta Ar \Big/ Xe \quad (5)$$

where *i* and *j* refer to Kr or Xe isotopes and ME_{ij} refers to the matrix effect associated with the ratio of isotopes *i* and *j*. All δ values in equations (4) and (5) are reported with respect to the working

reference gas (R25).

We empirically determined optimal *ME* values by minimizing disagreement between measured AEW isotope ratios (normalized to the mean of air standards) and high-precision published solubility equilibrium values in freshwater [13]. It is important to note that all measurements (samples and both AEW and air standards) are corrected for matrix effects using the same *ME* values. This approach yields well constrained *ME* values and provides a straightforward way to estimate error in the *ME* correction, by accounting for the combined errors of air standards, AEW standards, and uncertainty in the published solubility equilibrium values. Individual isotope ratio *ME* values and their associated uncertainties are provided in Table 3. We also apply this approach to correct measured elemental ratios for matrix effects in the same manner, by using precisely constrained solubility equilibrium data [14].

We attempted to independently evaluate these *ME* values by adding varying amounts of ultra-high purity (UHP) Ar to aliquots of the secondary reference gas R0 and analyzing these mixtures against the common reference gas R25. As shown in Fig. 4, we observe remarkably close agreement between these Ar-addition tests and the *ME* slopes independently determined by optimizing air-normalized AEW isotope ratios to known solubility equilibrium values for the two Kr isotope ratios measured in this study. For Xe isotopes, we observe the same pattern of *ME* values (Supp. Fig. S1; large values for $^{128}Xe/^{129}Xe$ and $^{136}Xe/^{129}Xe$, low values for $^{130}Xe/^{129}Xe$ with no obvious mass dependence). However, we find that (i) *ME* values determined via Ar addition are slightly higher than air-water determined *ME* values (Supp. Fig. S1), (ii) the offset is clearly mass dependent (Supp. Fig. S2), and (iii) the Xe/Kr ratio of these Ar-enriched samples increases linearly with the Ar/Kr (or Ar/Xe) ratio (Supp. Fig. S3). Together, these lines of evidence indicate that there must be a small, but non-negligible, amount of heavy-isotope-enriched Xe in the UHP Ar gas. Based on these findings, we urge caution for the use of UHP Ar in other Xe-related experiments, and we speculate that the highly adsorptive nature of Xe may explain its trace presence in supposedly pure Ar.

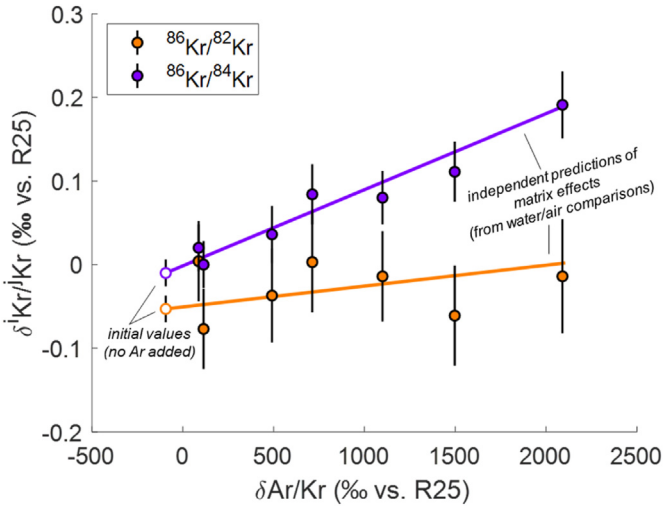

Fig. 4. Independent evaluation of Kr isotope matrix effects. Markers show data for experiments in which UHP Ar was added to aliquots of reference gas R0 and analyzed against reference gas R25. Solid lines show the expected change in Kr isotope ratios as a function of δAr/Kr using matrix effect values (*ME*) determined from air-normalized AEW measurements. For clarity, we emphasize that these lines are independent expectations; they are not lines of best fit to the data points shown in this figure. The agreement between the data and expectations thus provides independent confirmation of our AEW-based determination of *ME* values. Error bars indicate ±2σ.

2.3.3. Pressure imbalance sensitivity

Measured isotope ratios can be slightly biased by pressure imbalances between sample and reference bellows during analysis. Following prior work [9,11] we correct for biases due to pressure imbalance in the following manner:

$$\delta_{PI-corr} = \delta_{meas} - PIS \times PI \quad (6)$$

where $\delta_{PI\text{-}corr}$ is a corrected isotopic or elemental ratio δ value, *PIS* is the pressure imbalance sensitivity for that particular ratio and PI is the pressure imbalance, defined using the ^{40}Ar beam intensity:

$$PI = \frac{V_{40,SA}}{V_{40,R}} - 1 \quad (7)$$

where $V_{40,SA}$ and $V_{40,R}$ refer respectively to sample and reference gas mean ^{40}Ar beam intensities over the course of a measurement block. We determined mean *PIS* values for each isotope ratio in this study by regressing δ versus *PI* independently for each sample (recall that a typical sample involves 6, 8, and 12 blocks of Ar, Kr, and Xe measurements, respectively, for which pressure is rebalanced each time). *PIS* values are remarkably small (Table 2) and, for an entire sample measurement, result in isotope ratio corrections on the order of 0.001‰, since typical *PI* values for individual blocks are several ‰ (typically randomly distributed around zero). The large number of blocks we analyze per sample leads to very small mean *PI* values and thus small corrections for each sample.

2.3.4. Interference from ^{40}Ar tail

Due to dispersion of ion energies, a small fraction of the ions generated for any analyte will enter the flight tube at a slower velocity and thus experience additional deflection and interfere with other analytes that have lower ratios of mass to charge (*m/z*). Interference from such a low-mass tail is often negligible, except in instances for which there are analytes of interest that are orders-of-magnitude less abundant than an analyte with a slightly higher *m/z*. The measurement of Ar isotopes is an example one such instance, as ^{40}Ar is ~300 times more abundant than ^{36}Ar and ~1500 times more abundant than ^{38}Ar in air. Because only 3 Faraday cups are needed to measure the three stable Ar isotopes, multiple Faraday cups that are used for Kr and Xe analysis are unused in the Ar gas configuration. Here we introduce a first-order approach to resolve the low-mass ^{40}Ar tail using these additional Faraday cups and correcting ^{38}Ar and ^{36}Ar accordingly. We implemented ^{40}Ar tail

Table 3
Matrix effect (ME) corrections, their associated uncertainty estimates, and internal uncertainty estimates for Kr and Xe isotope ratios measured in air-like samples (δAr/Kr = 800‰; δAr/Xe = 2400‰; vs. R25) or ^{40}Ar-rich volcanic gases (δAr/Kr = 10000‰; δAr/Xe = 10000‰; vs. R25).

	$^{86}Kr/^{82}Kr$	$^{86}Kr/^{84}Kr$	$^{136}Xe/^{129}Xe$	$^{134}Xe/^{129}Xe$	$^{132}Xe/^{129}Xe$	$^{131}Xe/^{129}Xe$	$^{130}Xe/^{129}Xe$	$^{128}Xe/^{129}Xe$
ME corr$_{air}$ (‰)	0.020	0.073	0.358	0.295	0.204	0.386	0.031	0.595
$\sigma_{int,air}$ (‰)	0.030	0.017	0.079	0.059	0.061	0.076	0.076	0.136
$\sigma_{ME,air}$ (‰)	0.013	0.009	0.022	0.024	0.014	0.026	0.026	0.038
ME corr$_{volc}$ (‰)	0.250	0.910	1.490	1.230	0.850	1.610	0.130	2.480
$\sigma_{int,volc}$ (‰)	0.074	0.042	0.142	0.106	0.110	0.137	0.137	0.245
$\sigma_{ME,volc}$ (‰)	0.160	0.110	0.090	0.100	0.060	0.110	0.110	0.160

detection on two IRMS instruments in the Seltzer lab: a Thermo 253 plus and a Thermo 253, each with 10 Faraday cups but slightly different configurations, such that 4 intermediate mass cups (between 36 and 40 *m/z*) are available for ^{40}Ar tail detection on the 253 plus while 5 cups are available on the 253. Fig. 5 demonstrates the ability of these intermediate mass cups to detect the low-mass ^{40}Ar tail and shows the magnitude of isobaric interference at ^{38}Ar and ^{36}Ar at various run pressures of a gas with an atmospheric Ar isotope composition.

Due to the curvature of the ^{40}Ar tail in *m/z* space, the interference is not constant with run pressure. At higher run pressures (and correspondingly higher beam intensities for all isotopes), the fractional ^{40}Ar tail interference on the ^{38}Ar and ^{36}Ar beams increases (Fig. 5). Because the fractional interference scales quite linearly with run pressure, the existing (linear) pressure imbalance correction (Section 2.3.3.) effectively removes any bias on δ^{38}Ar/^{36}Ar caused by differential tail interferences between sample and reference gases, as long as the ^{40}Ar/^{36}Ar (or ^{40}Ar/^{38}Ar) ratios of sample and reference gases are similar. Indeed, we find that *PIS* values for ^{38}Ar/^{36}Ar are reduced from 0.0023 ± 0.0001 to 0.0001 ± 0.0001 when a tail correction is made to the ^{38}Ar and ^{36}Ar beam intensities prior to determination of *PIS*. For this reason, prior studies have indirectly corrected for ^{40}Ar tail interference by correcting for pressure imbalance, since these studies involved ice core air bubbles and groundwater, both of which have air-like Ar isotope ratios (e.g., Refs. [20,21]; [36]; [22].

However, for volcanic gases, in which ^{40}Ar/^{36}Ar ratios can be over an order of magnitude higher than in air (e.g., Ref. [23], pressure imbalance corrections will not remove the effect of ^{40}Ar interference from the ^{38}Ar/^{36}Ar ratio (if a reference gas with air-like Ar isotopes is used). Instead, a direct correction for ^{40}Ar tail interference is essential, such that a fitted curve constrained by intermediate mass measurements between *m/z* 36 and 40 is evaluated at *m/z* 38 and 36 to estimate interference (Fig. 5). To provide a sense of scale for the magnitude of ^{38}Ar/^{36}Ar bias due to ^{40}Ar interference we refer to Fig. 5, in which the ^{40}Ar tail is shown to account for ~1% of the ^{38}Ar beam (in an air-like reference gas) at a run pressure of 30 mbar and a corresponding ^{40}Ar beam intensity of ~3600 mV on the Thermo MAT 253 used for this analysis. If one were to analyze a volcanic gas sample with a ^{40}Ar/^{36}Ar ratio of ~600 (twice the atmospheric ratio) by pressure balancing on ^{40}Ar, the sample gas ^{38}Ar and ^{36}Ar beams would be roughly half as intense as the reference gas beams. Consequently, because the ^{40}Ar tail is identical between sample and reference gases (because pressure balancing is performed using ^{40}Ar), the fractional interference of the ^{38}Ar beam in the volcanic gas sample would be ~2%, leading to a bias of +10‰ (1%) in the uncorrected δ^{38}Ar/^{36}Ar value (slight interference of ^{36}Ar is neglected in this example for the sake of simplicity). Based on goodness of fit between fitted ^{40}Ar tail curves and measured intermediate mass beam intensities, we conservatively estimate that our first-order approach accurately removes ^{40}Ar tail interference with a residual bias of less than 5% of the original interference. For volcanic gas samples have ^{40}Ar/^{36}Ar of less than twice the atmospheric value (which is very common due to subsurface mixing with air-derived Ar in groundwater), we suggest that this first order tail-correction permits interpretation of ^{38}Ar/^{36}Ar at the sub-‰ level in those samples. However, considerably more work is required to develop and rigorously evaluate a ^{40}Ar tail correction for samples with ^{40}Ar/^{36}Ar that exceed the atmospheric ratio by an order of magnitude. For such samples, the influence of instrumental non-linearity on the ^{38}Ar and ^{36}Ar beams may also be appreciable. Evaluation of ^{40}Ar tail corrections either by adding pure ^{40}Ar to aliquots of reference gas or by cross-instrument comparison of ^{40}Ar-enriched gas samples is also key. We note that using a double-focusing IRMS is another possible approach to limiting the influence of the ^{40}Ar tail. Future work may benefit from implementing several of these strategies to improve ^{40}Ar tail correction.

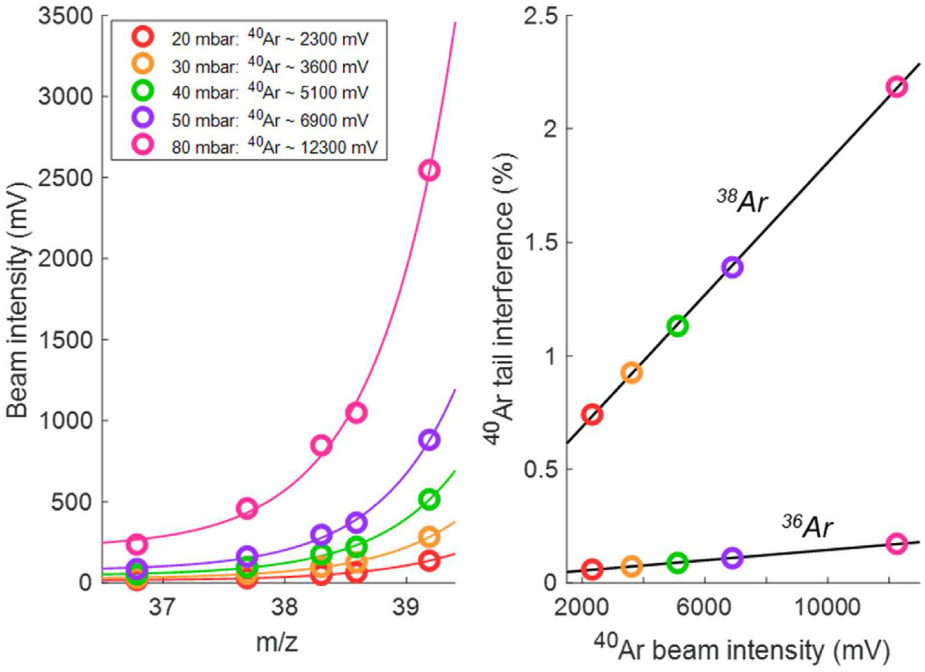

Fig. 5. Detection of ^{40}Ar tail on MAT 253 using 5 Faraday cups with intermediate *m/z* between ^{36}Ar, ^{38}Ar, and ^{40}Ar cups. On the left panel, measured beam intensities (open circles) at each cup and fitted ^{40}Ar tail curves (exponential fit) are shown for a reference can with air-like Ar isotope ratios analyzed at different run pressures. On the right panel, the fractional interference predicted (using the fitted curves) at ^{38}Ar and ^{36}Ar due to the ^{40}Ar tail is shown to increase with ^{40}Ar beam intensity (each marker corresponds to a different run pressure).

3. Results and discussion

3.1. Adsorption/desorption effects

A central component of this new technique is the transfer of Ar, Kr, and Xe gas using dual-valve dip tubes containing silica gel in a small chamber. The reproducibility of air and AEW standards (e.g., ±0.007‰ 1-σ precision for $\delta^{40}Ar/^{36}Ar$ in 26 air standards) is equivalent to the reproducibility of reference can versus can measurements and is on par with previous IRMS noble gas studies that have used liquid helium. This suggests that the use of silica gel does not reduce isotopic precision. However, it is important to fully understand whether, and by how much, the adsorption and subsequent desorption of Ar, Kr, and Xe may reproducibly fractionate isotopic and elemental ratios. Crucially, because air standards and samples are processed and analyzed identically, any reproducible fractionation should cancel when samples are normalized to air. Nonetheless, to gain awareness of the potential limitations of this technique, we carried out a suite of experiments using different absorbents and equilibrating in an isothermal bath at various temperatures. In each of these experiments, aliquots of a well characterized secondary reference gas were transferred into a dual-valve dip tube at 77 K, which was then closed at valve VT1 (Fig. 1) and placed in a water bath, leaving valve VT2 open for a minimum of 3 h for desorption and equilibration, following the same method for all samples and standards (Section 2.1). Valve VT2 was then closed upon removal of the dip tube from the bath, and the gas between valves VT1 and VT2 was analyzed.

Fig. 6 shows the results of dip tube fractionation experiments (n = 6) carried out using ~4 g of silica gel and a bath temperature 30 °C. All reported fractionation is given with respect to the mean of R0 measurements from aliquots sampled directly from the reference can (i.e., with the can itself attached to the sample side of the dual-inlet system). We observe no statistically significant fractionation of Ar isotopes, with mean offsets in $^{40}Ar/^{36}Ar$ and $^{38}Ar/^{36}Ar$ of −0.002 ± 0.006‰ and 0.002 ± 0.006‰, respectively (±2 SE). Based on this lack of fractionation and correspondence between measured and expected total gas pressures, we conclude that Ar must be quantitatively trapped on silica gel at 77 K and quantitatively desorbed at 30 °C. We find highly reproducible fractionation of elemental ratios, such that aliquots of R0 trapped on silica gel and released at 30 °C have Kr/Ar and Xe/Ar offsets of −27.969 ± 0.198‰ and −152.410 ± 0.622‰, respectively (±2 SE), from the mean of direct aliquots from the R0 can. Assuming Ar is quantitatively desorbed from the silica gel, this implies that ~2.8% of Kr and ~15.2% of Xe remain adsorbed at equilibrium at 30 °C. We find small, yet reproducible and statistically significant, isotope effects for Kr and Xe associated with this incomplete equilibrium desorption that favors the heavy isotopes by 0.0103 ± 0.0012‰ amu^{-1} and 0.0085 ± 0.0024‰ amu^{-1}, respectively (±2 SE; Fig. 6).

Only the high reproducibility, not the magnitude, of these isotope and elemental ratio effects is relevant for methodological focus of this study since samples and standards are processed identically. Nonetheless, here we briefly consider the physical origin of these Kr and Xe isotope effects. We assume that trapping of Kr and Xe in aliquots of R0 gas at 77 K is quantitative because Ar trapping appears to be quantitative and Kr and Xe should have higher adsorptivities than Ar. We can also rule out the possibility of incomplete equilibration leading to kinetic fractionation, both because we would expect that incomplete adsorption or desorption would favor the light isotopes and because we observe no relationship between equilibration time and Kr or Xe isotope ratios across air and AEW standard measurements equilibrated at 30 °C for time periods ranging from 3 h to 2 days. Thus, the observed heavy-isotope enrichment of Kr and Xe in the dip tubes implies that the light isotopes of these gases are preferentially adsorbed on silica gel at equilibrium at 30 °C. Accounting for the fractions of Kr and Xe that remain adsorbed at equilibrium (i.e., ~2.8 and 15.2% respectively), we can estimate equilibrium adsorption fractionation factors, α_{eq} (where $\alpha_{eq} = R_{ads}/R_{gas}$, R_{ads} and R_{gas} are adsorbed and gas phase isotope ratios, respectively, and R is defined with a heavy isotope in the numerator and light isotope in the denominator with a 1-amu mass difference). For 30 °C adsorption on silica gel, $\alpha_{eq} = 0.99963 \pm 0.00004$ ($\varepsilon_{eq} = -0.37 \pm 0.04$‰ amu^{-1}, ±2 SE) for Kr isotopes and $\alpha_{eq} = 0.99994 \pm 0.00002$ ($\varepsilon_{eq} = -0.06 \pm 0.02$‰ amu^{-1}, ±2 SE) for Xe isotopes. Past studies carried out at lower analytical precision using static noble gas mass spectrometers have found minimal fractionation of Xe isotopes due to adsorption [24,25]. For example, Marrocchi and Marty [25] find the same sign and approximate magnitude of Xe isotopic fractionation (~-0.2‰

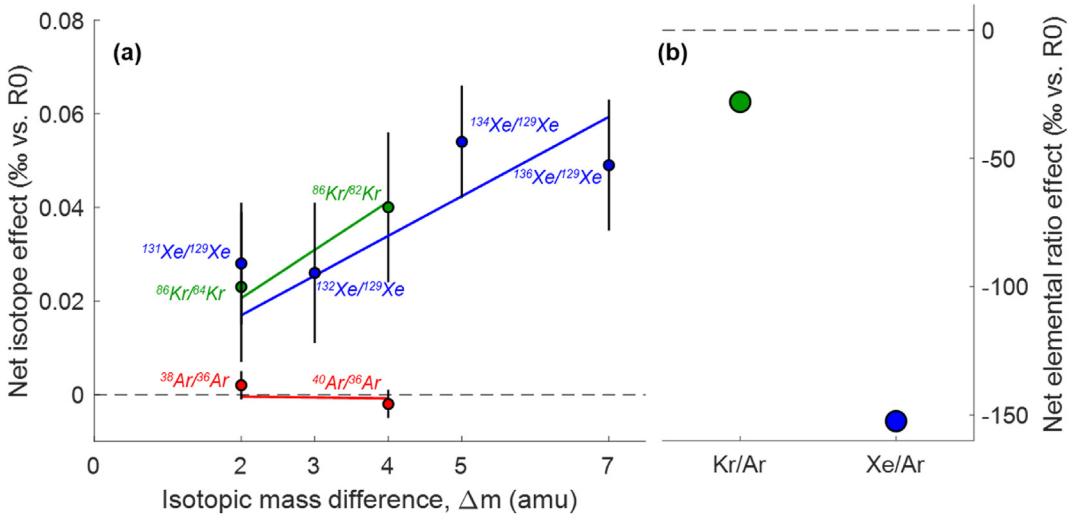

Fig. 6. Isotopic and elemental offset induced by dual-valve dip tubes containing silica gel with adsorption at 77 K and equilibrium desorption at 30 °C. In panel a, net isotope effects for Ar, Kr, and Xe isotope ratios are shown against isotopic mass difference with linear trend lines indicating mass dependency ($^{128}Xe/^{129}Xe$ and $^{130}Xe/^{129}Xe$ are not shown due to low abundance and thus higher uncertainties). In panel b, the net offset in elemental ratios is shown (error bars are substantially smaller than markers: ~0.2 and 0.6‰). All error bars indicate ±1 SE (combined error from measurement of R0 aliquots from dip tubes and directly from can).

amu^{-1}) due to equilibrium adsorption on kerogen and montmorillonite, and Bernatowicz & Podosek [24] find no statistically significant fractionation of Xe isotopes adsorbed on charcoal at lower (order ‰) statistical precision. Bernatowicz and Podosek [24] also derive theoretical expectations for isotopic fractionation due to equilibrium adsorption, predicting small effects (order ‰ amu^{-1} or below) that favor the light isotope in the adsorbed phase. Our estimated fractionation factors for Kr and Xe equilibrium adsorption on silica gel are therefore consistent both with prior experiments and theory.

While developing this new technique, we carried out tests with different adsorbent materials in the dual-valve dip tubes equilibrated at water bath temperatures ranging from 30 to 80 °C. In each experiment, aliquots of the same reference gas were trapped in a dip tube immersed in liquid nitrogen (77 K), and the dip tube was subsequently equilibrated for a minimum of 3 h in the water bath before valve VT2 was closed and the equilibrated gas between VT1 and VT2 was analyzed on a MAT 253 in the Seltzer lab for Ar isotope ratios, Kr/Ar, and Xe/Ar. In total we carried out experiments with dip tubes containing ~4 g of silica gel, zeolite (molecular sieve 13X: 10 Å pores), or activated charcoal. Fig. 7 summarizes the results of these experiments, which are reported relative to experiments with the silica gel dip tube at 30 °C.

As shown in Fig. 7, we find no statistically significant fractionation of Ar isotopes as a function of temperature or adsorbent material, suggesting that Ar is likely quantitatively adsorbed at 77 K and desorbed at temperatures ≥30 °C. Kr/Ar and Xe/Ar ratios, however, do exhibit substantial differences in relation to adsorbent material and equilibration temperature. At all temperatures, Kr/Ar and Xe/Ar ratios are highest when silica gel-containing dip tubes are used and lowest for charcoal-containing dip tubes. Given that ~15.2% of Xe is found to remain adsorbed on silica gel at equilibrium at 30 °C (Fig. 6), the observed Δδ value of ~-825‰ for charcoal at 30 °C (Fig. 7) implies that only ~2.7% of Xe is desorbed, with ~97.3% remaining adsorbed at equilibrium. We find apparent temperature sensitivities for Kr/Ar and Xe/Ar, respectively, of ~0.36‰ K^{-1} and 2.21‰ K^{-1} for silica gel, ~0.76‰ K^{-1}and 4.94‰ K^{-1} for zeolite, and ~3.05‰ K^{-1} and 7.90‰ K^{-1} for charcoal. (Note that the above values are linear regression coefficients and are thus approximations, as there is slight curvature to the temperature trend lines as shown in Fig. 7.)

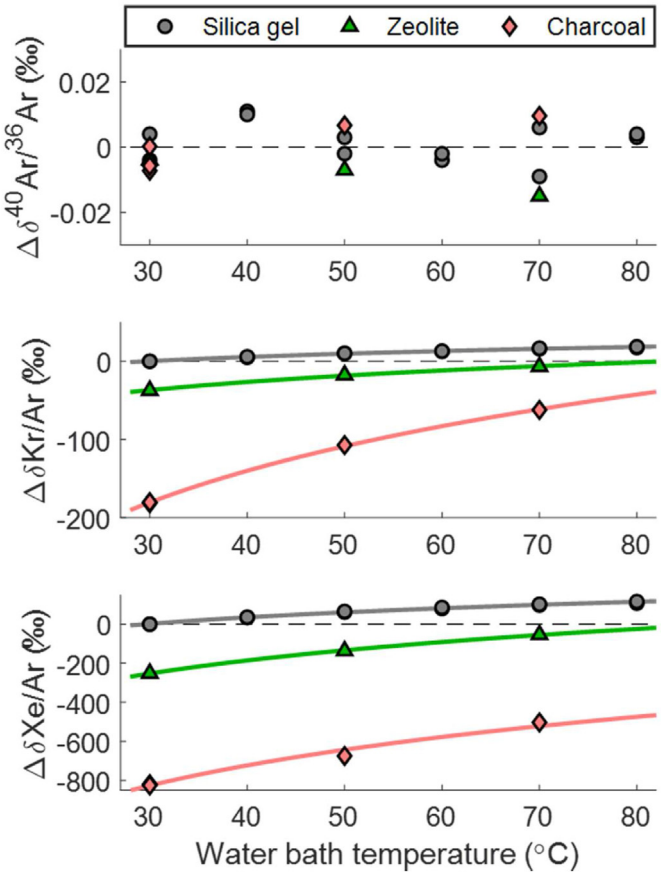

Fig. 7. Effects of using different absorbent materials at varying equilibration temperatures on measured ^{40}Ar/^{36}Ar, Kr/Ar, and Xe/Ar ratios. All data are reported as deviations (Δδ) from the mean of experiments carried out with silica gel at 30 °C. In other words, $\Delta\delta = R_{meas}/R_{Si30} - 1$, where R_{meas} is a measured isotopic or elemental ratio and R_{Si30} is that ratio measured on a silica gel-containing dip tube at 30 °C. Solid lines are logarithmic temperature trend lines for experiments carried out with each material.

There are several important implications from these adsorption/desorption experiments. First, the lower equilibrium absorptivities and temperature sensitivities of both Kr and Xe on silica gel justify its use for gas transfer in dip tubes in our new technique, instead of other common adsorbent materials (at least charcoal and zeolite, which we tested). That is, low equilibrium adsorption of Kr and Xe at 30 °C leaves more Kr and Xe in the dip tube available for analysis, while low temperature sensitivities reduce the need for stringent regulation of the water bath temperature. Second, the observations of small equilibrium isotope effects (Fig. 6) and high reproducibility of measured isotope ratios further support the use of silica gel-containing dip tubes as a viable approach for transferring Ar, Kr, and Xe for high-precision IRMS isotope ratio analyses. Finally, although silica gel-containing dip tubes exhibit the smallest Kr/Ar and Xe/Ar temperature sensitivities, we caution against using this technique for applications in which high-precision elemental ratio measurements are needed, such as ice-core based reconstructions of mean ocean temperature where signals of interest in Kr/Ar and Xe/Ar occur at the order-0.1‰ level [26–28]. However, for applications in groundwater and seawater, where solubility-related signals of interest in Kr/Ar and Xe/Ar ratios occur at the order-1‰ level [17,18,29–31], regulation of water bath temperatures to within ~0.1 °C is both practical and adequate for measuring elemental ratios at sufficiently high precision.

3.2. Importance of correcting for background error

In section 2.3.1, we described observations of background error-induced scatter in measured Xe isotope ratios and outlined a protocol for correcting Xe isotope ratios accordingly. Here we briefly demonstrate the importance of correcting trace Xe isotope ratios for background error effects, speculate on the origin of background errors, and suggest an approach for reducing their magnitude.

The sensitivity of a given Xe isotope ratio to error in the subtracted background value is related to both the abundance of the isotopes involved and the difference in Xe/Ar ratios between sample and reference gases. For this reason, we expect that the ^{128}Xe/^{130}Xe ratio in low Xe/Ar samples would be the most sensitive to background errors. In volcanic gas samples, the ^{128}Xe/^{130}Xe ratio is crucial for correcting other Xe isotopes for mass-dependent fractionation since ^{128}Xe and ^{130}Xe are the only non-radiogenic and non-fissiogenic isotopes analyzed in our new IRMS technique. Coincidentally, the Xe/Ar ratio will also be low in volcanic gas samples due to the abundance of radiogenic ^{40}Ar. Thus, we expect that background corrections will be most important for volcanic samples. To demonstrate the relative importance of background corrections, in Fig. 8 we show anomalies of δ^{128}Xe/^{130}Xe in water, air, and volcanic gas samples relative to their respective means for both background-corrected and uncorrected data. The volcanic gas samples (n = 3) refer to three replicate samples collected from

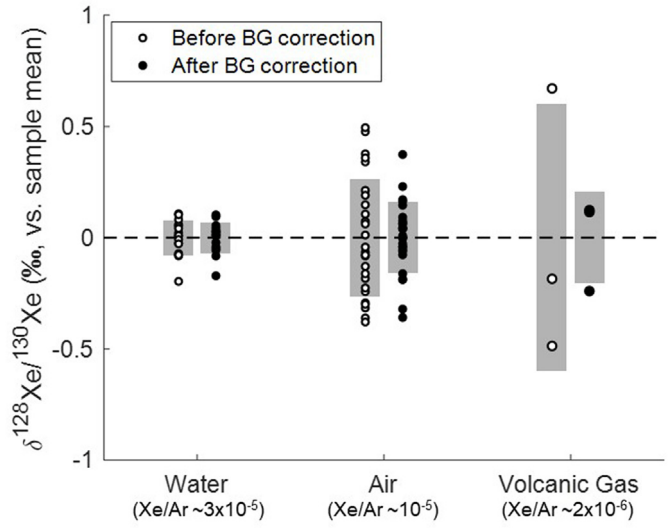

Fig. 8. Reproducibility of water (AEW), air, and volcanic gas $^{128}Xe/^{130}Xe$ ratios with and without background (BG) corrections. As expected, we find that making background corrections (i.e., via equations (2) and (3)) substantially improves the reproducibility of samples with lower Xe/Ar ratios.

Mount Etna (Italy) via the Giggenbach technique [23,32,33] in which ~10^2–10^3 L of CO_2-rich volcanic gas is bubbled into an evacuated 1.5-L flask filled with 200 mL of 5 M NaOH solution such that CO_2 dissolves and the headspace is concentrated in other gases (including the noble gases). The headspace is then analyzed following the technique outlined in this study. The Mount Etna samples have $^{40}Ar/^{36}Ar$ ratios of ~1900 and Xe/Ar ratios of ~2×10^{-7}. We find that 1-σ reproducibility improves from 0.079 to 0.069‰ for AEW standards, from 0.264 to 0.160‰ for air standards, and from 0.601 to 0.208‰ for volcanic gas samples.

To reduce the magnitude of background corrections, it is first important to understand the underlying source of error. If the error in the measured background voltages on each Faraday cup is governed purely by Johnson noise, the background noise should be white. Thus, by increasing the background integration time (t_{int}), the error should correspondingly decrease with $t_{int}^{1/2}$ in theory. In practice, however, if the background noise is red then increasing t_{int} may not substantially reduce the error. To test this, we carried out a background scan at 0.15-s resolution for ~30 min and investigated the power spectrum of the ^{128}Xe Faraday cup (10^{13} Ω resistor; Supp. Fig. S4). We find a broad peak at ~0.2 Hz and sharp peaks near 3 and 3.6 Hz. The standard error of the background scan over a period of 22 s (equivalent to our default background integration time) is ~0.075 mV, which is somewhat smaller than the standard deviation of BG' (~0.10 mV). The fact that the default integration time only captures 4.5 cycles of the ~0.2 Hz^{-1} oscillation may explain why the standard deviation of BG' is somewhat higher than the equivalent standard error from the ~30-min background scan. We therefore suggest that increasing the background integration time prior to analysis of Xe blocks is a viable solution to reduce error in background Faraday cup voltages. Practically, a longer background scan (e.g., we suggest ~6 min) should reduce background errors and associated Xe isotope anomalies (e.g., by a factor of ~4) without wasting a substantial amount of gas from the bellows. Additionally, even with an increased background integration time, we recommend monitoring background voltages over time and correcting in the manner described in section 2.3.1, as these corrections may remain important for samples with low Xe/Ar ratios.

3.3. Uncertainty analysis

In other IRMS noble gas studies, uncertainty of individual sample measurements has often been estimated using the pooled standard deviation of replicate measurements [9,13]. Such an approach implicitly incorporates error stemming from shot noise (ion counting statistics), pressure imbalance corrections, and any fractionation related to gas collection, processing, storage, or transfer. This approach does not, however, consider the error associated with matrix effect corrections, since replicate samples have the same elemental ratios and thus the same matrix effects. Because volcanic gas samples are often difficult to collect as identical replicates, and matrix effect corrections can be large due to high Ar/Kr and Ar/Xe ratios, an independent method for estimating single sample uncertainty that considers error in matrix effect corrections is needed.

We assume that the leading sources of uncertainty (after implementing all corrections described in section 2.3) arise from (a) shot noise/ion counting statistics and (b) matrix effect corrections. Pressure imbalance corrections are often very small (order 0.001‰) and thus their associated error is likely negligible. Given the reasonably close agreement between the expected background error from the ~30-min 0.15-s resolution background scan (0.075 mV for ^{128}Xe) and actual sample-to-sample background anomalies (BG') calculated based on deviations from the long-term trend (e.g., 0.10 mV for ^{128}Xe), any residual error in background corrections must be quite small. Finally, we note that air standard and reference can vs. can reproducibilities are quite similar. For example, σ = 0.007‰ for $^{40}Ar/^{36}Ar$ in air and 0.006‰ in reference can vs. can measurements. Since Ar isotopes are the most sensitive of all measured isotope ratios to leakage or incomplete transfer, human error in sample processing is similarly unlikely to be a leading source of error.

Thus, to estimate uncertainty, we expect that internal uncertainty (σ_{int}), arising from ion counting statistics, should scale with inverse square root of ion beam intensities, and matrix effect-related uncertainty (σ_{ME}) can be determined from the combined standard errors of air standards, AEW standards, and the published solubility fractionation factors for each of the Kr and Xe isotope ratios analyzed in this study. These matrix effect uncertainty estimates are provided in Table 2. Since σ_{int} and σ_{ME} are not correlated, we estimate the total uncertainty of any Kr or Xe isotope measurement in a single sample from the quadrature sum of these two values. For high Ar/Kr and Ar/Xe ratios (e.g., due to higher abundances of ^{40}Ar in volcanic samples), both sources of uncertainty are substantial: σ_{int} is high because Kr and Xe ion beams are small, and σ_{ME} is high because the ME correction is large at high values of Ar/Xe and Ar/Kr. To illustrate this point, Fig. 9 shows estimates of the combined and individual sources of uncertainty for $^{86}Kr/^{82}Kr$ and $^{136}Xe/^{129}Xe$ as a function of the Ar/Kr and Ar/Xe ratios. We find that the uncertainty in the matrix effect correction becomes the leading source of error for Kr isotopes once the Ar/Kr ratio of a sample is ≥ ~3.5 times that of reference can (i.e., δAr/Kr ~2500‰ vs. R25). For Xe isotopes, internal ion counting is the leading source of error even once the Ar/Xe ratio is an order of magnitude higher than the reference can. For future studies of volcanic samples measured via IRMS, this approach to decomposing sources of error and estimating sample-specific uncertainties will be important in the ultimate interpretation of measured Kr and Xe isotope ratios.

3.4. Consistency of air sampling methods

The well-mixed atmosphere is the ultimate standard against which all measured isotope ratios are compared (e.g., equation (1)). For this reason, it is crucial to ensure that the collection, processing,

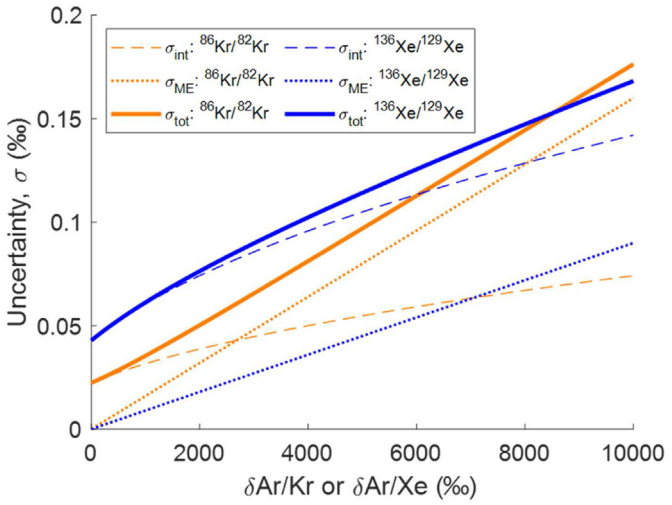

Fig. 9. Estimated total 1-σ uncertainty (σ_{tot}) and uncertainties arising from matrix effect corrections (σ_{ME}) and internal ion counting (σ_{int}) for $^{86}Kr/^{82}Kr$ and $^{136}Xe/^{129}Xe$ as a function of δAr/Kr or δAr/Xe (reported with respect to the reference gas R25).

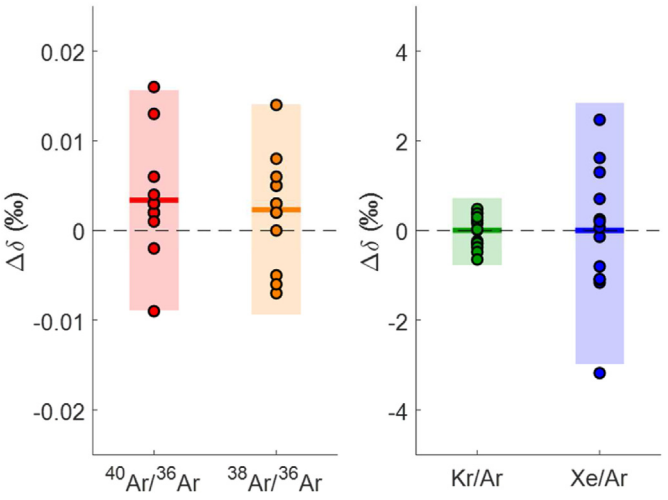

Fig. 10. Deviations (Δδ) of air collected via the Giggenbach method from the mean of air standards. Solid lines indicate mean offsets for each ratio, and shaded regions indicate ±2-σ ranges.

and analysis of air standards is both precise and accurate. The sampling method for air standards is described in section 2.1 and the precision of measured isotope ratios is summarized in Table 2. To test the robustness of this sampling technique, we collected additional air standards using two separate methods. First, we collected outside air by continuously pumping air into a flow-through 2-L flask at ~4 L min^{-1} using a Metal Bellows MB-41 pump following standard methods (e.g., Severinghaus and Grachev, 2003). In four ~100 mL aliquots, we observed no statistically significant fractionation with respect to the mean of n = 26 lab air aliquots. For example, we found a mean offset of −0.004 ± 0.010‰ (±2 SE) for $^{40}Ar/^{36}Ar$ in outside air aliquots versus lab air. We note that $^{40}Ar/^{36}Ar$ should be the most sensitive of any measure isotope ratios to any kinetic or thermal fractionation associated with the different methods of sample collection. Second, we collected lab air following by bubbling air (pumped using the same Metal Bellows MB-41 pump) into pre-evacuated inverted (valve-side down) 1.5-L flasks with flow-through necks and teflon stopcocks (at the bottom), filled with ~200 mL of 5 M NaOH solution, following the method of Giggenbach [33]. While the Giggenbach sampling technique is well established, we are not aware of any study that has attempted to quantify the potential for either kinetic fractionation associated with bubbling of gas through the NaOH solution or fractionation due to dissolution of gases in NaOH. Multiple ~100 mL aliquots were collected from each Giggenbach bottle, and bottles were stored for varying periods of time up to four months before sample processing and analysis for Ar isotopes and elemental ratios on the MAT 253. Fig. 10 shows the offsets of these ratios measured in Giggenbach air samples from the mean of lab air standards analyzed on that instrument. We find no statistically significant fractionation of $^{40}Ar/^{36}Ar$, $^{38}Ar/^{36}Ar$, Kr/Ar, or Xe/Ar with mean offsets of 0.003 ± 0.006‰, 0.002 ± 0.006‰, −0.028 ± 0.404‰, and −0.066 ± 1.863‰, respectively (±2 SE).

The close agreement between Giggenbach air samples, lab air standards, and outside air provides confidence in the accuracy of air measurements across all three techniques. The absence of any fractionation associated with the Giggenbach technique is encouraging for future applications of this technique to measure heavy noble gas isotopic and elemental ratios in CO_2-rich volcanic gas samples. These Giggenbach air sample tests also confirm the expectation that the solubility of Ar, Kr, and Xe must be extremely low in 5 M NaOH solution, as evidenced by the lack of any elemental or isotopic fractionation relative to air standards. We therefore suggest that the Giggenbach technique is a viable approach for collecting unfractionated volcanic gas samples, opening the door to IRMS measurements of heavy noble gases in mantle volatile-rich samples.

4. Conclusions

We have developed and tested a new, unified analytical technique for high-precision measurement of heavy noble gas isotope ratios in air, water, and volcanic gas samples. This method offers several key advantages and caveats. First, this technique eliminates the need for cryostats or liquid helium, using silica gel and dual-valve dip tubes as a convenient, inexpensive, and sustainable solution to gas transfer without sacrificing precision for isotope ratio measurements. Second, the implementation of new correction schemes for background errors, Ar tail interference, and matrix effects represents a step towards improving the accuracy of IRMS measurements in samples with substantially different composition than reference gases. Finally, for samples in which Xe/Ar and Kr/Ar ratios are entirely unknown prior to measurement (e.g., volcanic gases), this method opens the door to IRMS analysis. Until now, analyses of Kr and Xe isotopes in such samples have not been possible due to the stringent requirements for balanced pressure between sample and reference gases in a dual-inlet system. Moreover, the evaluation of the Giggenbach technique demonstrates that this approach constitutes a viable method for collecting concentrated noble gas samples from CO_2-dominated volcanic gas sources, enabling one to obtain sufficiently large samples for IRMS analysis (e.g., 1 mL_{STP} of ^{40}Ar).

There are several important limitations of this technique, as well as opportunities for future improvement. First, the order 0.1‰ sensitivity of Kr/Ar and Xe/Ar ratios to order 0.1 °C fluctuations in equilibration bath temperatures renders this silica gel/dual-valve dip tube approach unsuitable for applications in which high precision elemental ratios are required (e.g., for ice-core based mean ocean temperature reconstruction). However, for seawater, groundwater, and volcanic gas applications, Kr/Ar and Xe/Ar fluctuations at the 0.1‰ level do not preclude resolution of signals of interest. Second, it is conceivable that an adsorbent material exists or could be developed that quantitatively traps Ar, Kr, and Xe at

77 K while quantitatively releasing all three gases at room temperature. While silica gel is clearly the most suitable material of the three adsorbents we tested, future studies investigating other materials may identify a better adsorbent and would thus be worthwhile. Finally, while the first-order Ar tail correction we have implemented represents an important step toward eliminating this common source of isobaric interference, it could be improved upon in several ways. For example, the use of a double-focusing IRMS [34] may reduce or eliminate the low-energy Ar tail. Additionally, adding pure ^{40}Ar to known reference gas aliquots and testing for ^{38}Ar/^{36}Ar biases would represent a useful approach to evaluating and refining the Ar tail correction method we have introduced. However, we were unable to obtain sufficiently pure ^{40}Ar (enrichment factor > 10^4) from any commercial or scientific supplier for the present study. Ultimately, with a robust correction for ^{40}Ar tail interference, we suggest that this IRMS technique offers the potential to resolve longstanding questions about the origin of Earth's Ar through unprecedently accurate and precise measurements of the ^{38}Ar/^{36}Ar ratio of the mantle which, to date, has not been found to differ significantly from the atmosphere at the order-‰ level [35]. Building upon the strong foundation laid by prior methodological advances that facilitated IRMS measurements of air and ice core bubbles [9,11,12], we anticipate that this new technique - and future advances built upon it - will open the door to new applications of heavy noble gas isotopes in hydrology, oceanography, and mantle geochemistry.

Author statement

Alan Seltzer: Conceptualization, Methodology, Writing- Original draft preparation, Software, Funding acquisition, Project Administration, Data Curation, Investigation, Formal Analysis, Visualization, Resources; **David Bekaert:** Writing- Reviewing and Editing, Formal Analysis, Methodology, Data Curation, Visualization.

Declaration of competing interest

The authors declare that they have no known competing financial interests or personal relationships that could have appeared to influence the work reported in this paper.

Acknowledgements

This work benefitted substantially from helpful conversations with Ross Beaudette, Benni Birner, Sarah Shackleton, Jessica Ng, Jeff Severinghaus, Dempsey Lott, Bill Jenkins, and Michael Bender. We thank Josh Curtice for his help in fabricating and maintaining equipment used in this study, Peter Barry for kindly sharing resources that helped make the early stages of this work possible, and Delia Oppo and Weifu Guo for their generosity in sharing a Thermo MAT 253 that was reconfigured for noble gas measurements and used for part of this study. We thank Antonio Caracausi for his assistance in collecting three replicate samples of volcanic gas from Mt. Etna that were used in this study to assess the importance of background corrections. This work was supported by National Science Foundation awards OCE-2122427 and EAR-2102457, as well as the Andrew W. Mellon Foundation Endowed Fund for Innovative Research.

Appendix A. Supplementary data

Supplementary data to this article can be found online at https://doi.org/10.1016/j.ijms.2022.116873.

References

[1] J.J. Thomson, Bakerian lecture:—rays of positive electricity, Proc. R. Soc. Lond. - Ser. A Contain. Pap. a Math. Phys. Character 89 (1913) 1–20, https://doi.org/10.1098/RSPA.1913.0057.
[2] A.O. Nier, A mass spectrometer for isotope and gas analysis, Rev. Sci. Instrum. 18 (1947) 398–411, https://doi.org/10.1063/1.1740961.
[3] L.T. Aldrich, A.O. Nier, Argon 40 in potassium minerals, Phys. Rev. 74 (1948) 876, https://doi.org/10.1103/PhysRev.74.876.
[4] A.O. Nier, Some reminiscences of isotopes, geochronology, and mass spectrometry, Annu. Rev. Earth Planet Sci. 9 (1981) 1–17, https://doi.org/10.1146/annurev.ea.09.050181.000245.
[5] J.H. Reynolds, High sensitivity mass spectrometer for noble gas analysis, Rev. Sci. Instrum. 27 (1956) 928–934, https://doi.org/10.1063/1.1715415.
[6] I. McDougall, T.M. Harrison, Geochronology and Thermochronology by the 40Ar/39Ar Method, second ed., Oxford University Press, Oxford, 1999.
[7] M.A. Moreira, M.D. Kurz, Noble gases as tracers of mantle processes and magmatic degassing, in: The Noble Gases as Geochemical Tracers, Springer Berlin Heidelberg, Berlin, Heidelberg, 2013, pp. 371–391, https://doi.org/10.1007/978-3-642-28836-4_12.
[8] C.R. McKinney, J.M. McCrea, S. Epstein, H.A. Allen, H.C. Urey, Improvements in mass spectrometers for the measurement of small differences in isotope abundance ratios, Rev. Sci. Instrum. 21 (1950) 724–730, https://doi.org/10.1063/1.1745698.
[9] J.P. Severinghaus, A. Grachev, B. Luz, N. Caillon, A method for precise measurement of argon 40/36 and krypton/argon ratios in trapped air in polar ice with applications to past firn thickness and abrupt climate change in Greenland and at Siple Dome, Antarctica, Geochem. Cosmochim. Acta 67 (2003) 325–343, https://doi.org/10.1016/S0016-7037(02)00965-1.
[10] B. Bereiter, K. Kawamura, J.P. Severinghaus, New methods for measuring atmospheric heavy noble gas isotope and elemental ratios in ice core samples, Rapid Commun. Mass Spectrom. 32 (2018a) 801–814, https://doi.org/10.1002/rcm.8099.
[11] M.L. Bender, P.P. Tans, J.T. Ellis, J. Orchardo, K. Habfast, A high precision isotope ratio mass spectrometry method for measuring the O2N2 ratio of air, Geochem. Cosmochim. Acta 58 (1994) 4751–4758, https://doi.org/10.1016/0016-7037(94)90205-4.
[12] T. Sowers, M. Bender, D. Raynaud, Elemental and isotopic composition of occluded O_2 and N_2 in polar ice, J. Geophys. Res. 94 (1989) 5137, https://doi.org/10.1029/JD094iD04p05137.
[13] A.M. Seltzer, J. Ng, J.P. Severinghaus, Precise determination of Ar, Kr and Xe isotopic fractionation due to diffusion and dissolution in fresh water, Earth Planet Sci. Lett. 514 (2019b) 156–165, https://doi.org/10.1016/j.epsl.2019.03.008.
[14] W.J. Jenkins, D.E. Lott, K.L. Cahill, A determination of atmospheric helium, neon, argon, krypton, and xenon solubility concentrations in water and seawater, Mar. Chem. 211 (2019) 94–107, https://doi.org/10.1016/j.marchem.2019.03.007.
[15] S. Emerson, C. Stump, D. Wilbur, P. Quay, Accurate measurement of O2, N2, and Ar gases in water and the solubility of N2, Mar. Chem. 64 (1999) 337–347, https://doi.org/10.1016/S0304-4203(98)00090-5.
[16] K. Kawamura, J.P. Severinghaus, M.R. Albert, Z.R. Courville, M.A. Fahnestock, T. Scambos, E. Shields, C.A. Shuman, Kinetic fractionation of gases by deep air convection in polar firn, Atmos. Chem. Phys. 13 (2013) 11141–11155, https://doi.org/10.5194/acp-13-11141-2013.
[17] A.M. Seltzer, F.J. Pavia, J. Ng, J.P. Severinghaus, Heavy noble gas isotopes as new constraints on the ventilation of the deep ocean, Geophys. Res. Lett. 46 (2019c) 8926–8932, https://doi.org/10.1029/2019gl084089.
[18] A.M. Seltzer, J. Ng, W.R. Danskin, J.T. Kulongoski, R.S. Gannon, M. Stute, J.P. Severinghaus, Deglacial water-table decline in Southern California recorded by noble gas isotopes, Nat. Commun. 10 (2019a), https://doi.org/10.1038/s41467-019-13693-2.
[19] A.M. Seltzer, J.P. Severinghaus, B.J. Andraski, D.A. Stonestrom, Steady state fractionation of heavy noble gas isotopes in a deep unsaturated zone, Water Resour. Res. 53 (2017) 2716–2732, https://doi.org/10.1002/2016WR019655.
[20] M.L. Bender, B. Barnett, G. Dreyfus, J. Jouzel, D. Porcelli, The contemporary degassing rate of 40Ar from the solid Earth, Proc. Natl. Acad. Sci. U. S. A. 105 (2008) 8232–8237, https://doi.org/10.1073/pnas.0711679105.
[21] J.A. Higgins, A.V. Kurbatov, N.E. Spaulding, E. Brook, D.S. Introne, L.M. Chimiak, Y. Yan, P.A. Mayewski, M.L. Bender, Atmospheric composition 1 million years ago from blue ice in the Allan Hills, Antarctica, Proc. Natl. Acad. Sci. U. S. A. 112 (2015) 6887–6891, https://doi.org/10.1073/pnas.1420232112.
[22] Y. Yan, M.L. Bender, E.J. Brook, H.M. Clifford, P.C. Kemeny, A.V. Kurbatov, S. Mackay, P.A. Mayewski, J. Ng, J.P. Severinghaus, J.A. Higgins, Two-million-year-old snapshots of atmospheric gases from Antarctic ice, Nature 574 (2019) 663–666, https://doi.org/10.1038/s41586-019-1692-3.
[23] D.V. Bekaert, M.W. Broadley, A. Caracausi, B. Marty, Novel insights into the degassing history of Earth's mantle from high precision noble gas analysis of magmatic gas, Earth Planet Sci. Lett. 525 (2019), https://doi.org/10.1016/J.EPSL.2019.115766.
[24] T.J. Bernatowicz, F.A. Podosek, Adsorption and isotopic fractionation of Xe, Geochem. Cosmochim. Acta 50 (1986) 1503–1507, https://doi.org/10.1016/0016-7037(86)90324-8.
[25] Y. Marrocchi, B. Marty, Experimental determination of the xenon isotopic

fractionation during adsorption, Geophys. Res. Lett. 40 (2013) 4165–4170, https://doi.org/10.1002/grl.50845.
[26] B. Bereiter, S. Shackleton, D. Baggenstos, K. Kawamura, J. Severinghaus, Mean global ocean temperatures during the last glacial transition, Nature 553 (2018b) 39–44, https://doi.org/10.1038/nature25152.
[27] S. Shackleton, D. Baggenstos, J.A. Menking, M.N. Dyonisius, B. Bereiter, T.K. Bauska, R.H. Rhodes, E.J. Brook, V.V. Petrenko, J.R. McConnell, T. Kellerhals, M. Häberli, J. Schmitt, H. Fischer, J.P. Severinghaus, Global ocean heat content in the Last Interglacial, Nat. Geosci. 13 (2020) 77–81, https://doi.org/10.1038/s41561-019-0498-0.
[28] S. Shackleton, B. Bereiter, D. Baggenstos, T.K. Bauska, E.J. Brook, S.A. Marcott, J.P. Severinghaus, Is the noble gas-based rate of ocean warming during the younger dryas overestimated? Geophys. Res. Lett. 46 (2019) 5928–5936, https://doi.org/10.1029/2019GL082971.
[29] R.C. Hamme, S.R. Emerson, J.P. Severinghaus, M.C. Long, I. Yashayaev, Using noble gas measurements to derive air-sea process information and predict physical gas saturations, Geophys. Res. Lett. 44 (2017) 9901–9909, https://doi.org/10.1002/2017GL075123.
[30] R.C. Hamme, J.P. Severinghaus, Trace gas disequilibria during deep-water formation, Deep. Res. Part I Oceanogr. Res. Pap. 54 (2007) 939–950, https://doi.org/10.1016/j.dsr.2007.03.008.
[31] A.M. Seltzer, J. Ng, W. Aeschbach, R. Kipfer, J.T. Kulongoski, J.P. Severinghaus, M. Stute, Widespread six degrees celsius cooling on land during the last glacial maximum, Nature 593 (2021b) 228–232, https://doi.org/10.1038/s41586-021-03467-6.
[32] M.W. Broadley, P.H. Barry, D.V. Bekaert, D.J. Byrne, A. Caracausi, C.J. Ballentine, B. Marty, Identification of chondritic krypton and xenon in Yellowstone gases and the timing of terrestrial volatile accretion, Proc. Natl. Acad. Sci. U. S. A. 117 (2020) 13997–14004, https://doi.org/10.1073/PNAS.2003907117/-/DCSUPPLEMENTAL.
[33] W.F. Giggenbach, A simple method for the collection and analysis of volcanic gas samples, Bull. Volcanol. 39 (1975) 132–145, https://doi.org/10.1007/BF02596953.
[34] J.M. Eiler, M. Clog, P. Magyar, A. Piasecki, A. Sessions, D. Stolper, M. Deerberg, H.-J. Schlueter, J. Schwieters, A high-resolution gas-source isotope ratio mass spectrometer, Int. J. Mass Spectrom. 335 (2013) 45–56, https://doi.org/10.1016/j.ijms.2012.10.014.
[35] C.J. Ballentine, G. Holland, What CO2 well gases tell us about the origin of noble gases in the mantle and their relationship to the atmosphere, Philos. Trans. R. Soc. A Math. Phys. Eng. Sci. 366 (2008) 4183–4203, https://doi.org/10.1098/rsta.2008.0150.
[36] A.M. Seltzer, J.A. Krantz, J. Ng, W.R. Danskin, D.V. Bekaert, P.H. Barry, D.L. Kimbrough, J.T. Kulongoski, J.P. Severinghaus, The triple argon isotope composition of groundwater on ten-thousand-year timescales, Chem. Geol. 583 (2021a), https://doi.org/10.1016/J.CHEMGEO.2021.120458.